

X-RAY SPECTROSCOPY OF ABELL S1101 WITH CHANDRA, XMM-NEWTON AND ROSAT: BAND-PASS DEPENDENCE OF THE TEMPERATURE PROFILE AND SOFT EXCESS EMISSION

MASSIMILIANO BONAMENTE^{1,2} AND JUKKA NEVALAINEN^{3,4}

Draft version July 6, 2011

ABSTRACT

We present spatially-resolved spectroscopy of the galaxy cluster Abell S1101, also known as Sèrsic 159-03, with *Chandra*, *XMM-Newton* and *ROSAT*, and investigate the presence of soft X-ray excess emission above the contribution from the hot intra-cluster medium. In earlier papers we reported an extremely bright soft excess component that reached 100% of the thermal radiation in the R2 *ROSAT* band (0.2-0.4 keV), using the HI column density measurement by Dickey and Lockman. In this paper we use the newer Leiden-Argentine-Bonn survey measurements of the HI column density towards Abell S1101, significantly lower than the previous value, and show that the soft excess emission in Abell S1101 is now at the level of 10-20% of the hot gas emission, in line with those of a large sample of clusters analyzed by Bonamente et al. in 2002. The *ROSAT* soft excess emission is detected regardless of calibration uncertainties between *Chandra* and *XMM-Newton*. This new analysis of Abell S1101 indicate that the 1/4 keV band emission is compatible with the presence of WHIM filaments connected to the cluster and extending outward into the intergalactic medium; the temperatures we find in this study are typically lower than the WHIM probed in other X-ray studies. We also show that the soft excess emission is compatible with a non-thermal origin as the inverse Compton scattering of relativistic electrons off the cosmic microwave background, with pressure less than 1% of the thermal electrons.

Subject headings: galaxies: clusters: individual (Abell S1101); cosmology: large-scale structure of universe

1. INTRODUCTION

Evidence for an excess of soft X-ray radiation in clusters above the contribution from the virial gas was initially discovered by Lieu et al. (1996a,b) in the extreme ultra-violet ($h\nu \sim 0.1$ keV) with *EUVE*, and then confirmed with several other instruments, notably in the *ROSAT* 1/4 keV band (see Bonamente et al. 2002 for the analysis of a sample of 38 clusters, and Durret et al. 2008 for a recent review of the literature). The excess emission is usually modelled as an additional thermal component of lower temperature ($kT \sim 10^6 - 10^7$ K) or as a non-thermal power law. A plausible scenario for the soft excess is thermal emission from warm filaments seen in projection towards clusters (e.g., Mittaz et al. 2004; Bonamente et al. 2005), or from low-entropy dense gas within the cluster (Cheng et al. 2005). Alternatively, a non-thermal power law can be used to model the excess, indicative of relativistic electrons that scatter the CMB photons and emit by Compton scattering (e.g., Sarazin & Lieu 1998; Lieu et al. 1999). Other explanations are also viable, e.g. multi-temperature structure due to several mergers during the lifetime of a cluster (Lehto et al. 2010). Given the limited spectral resolution of the current CCD detector technology, it has not been possible to prove conclusively which additional model is a better fit to the data (see, e.g., Nevalainen et al. 2003;

Bonamente et al. 2005; Werner et al. 2007).

Among the factors that affect the detection of the soft excess emission, the column density of absorbing HI plays a primary role. In recent years, the Leiden-Bonn-Argentine survey (LAB) of Kalberla et al. (2005) has effectively superseded the Dickey & Lockman (1990) measurements, and significant differences between the two surveys are occasionally present. Among the clusters in which the excess has been reported in the literature, Abell S1101 is an outstanding case in that the Dickey & Lockman (1990) value of $N_H = 1.80 \times 10^{20}$ cm⁻² differs significantly from the LAB value of $N_H = 1.15 \times 10^{20}$ cm⁻². A lower N_H value implies less Galactic absorption, and therefore more of the detected soft X-ray flux from the cluster originates as the soft tail of the hot, virial gas, reducing the need for an additional emission component.

The goal of this paper is to perform a spatially-resolved spectroscopic study of Abell S1101 using the available data from *Chandra* and *XMM-Newton*, needed to measure the temperature of the hot gas, and *ROSAT*, needed to test whether at soft X-ray energies the radiation is consistent with the low-energy tail of the hot gas, or whether an excess of emission is present. This paper improves on the initial detection of the *ROSAT* soft excess in Abell S1101 by Bonamente et al. (2001) in two ways: the hot gas is measured from *Chandra* and *XMM-Newton* data that are much more sensitive to hot gas than the *ROSAT* observations alone, and the use of the new LAB value for N_H . The presence of a soft component in the spectrum is investigated by testing whether the best-fit temperature of the hot gas has a bandpass dependence, as observed in certain clusters (for example, Cavagnolo et al. 2008; Lehto et al. 2010,

¹ Physics Department, University of Alabama in Huntsville, Huntsville, AL 35899

² NASA National Space and Technology Center, Huntsville, AL 35899

³ Finnish Center for Astronomy with ESO, University of Turku, Väisäläntie 20, FI-21500, Piikkiö, Finland

⁴ Department of Physics, Dynamicum, P.O. Box 48, 00014 University of Helsinki, Finland

see Section 3), by modelling the hot gas with a single-temperature model and a two-temperature model to account for cooler gas seen in projection, and determine whether the soft X-ray flux lies above the prediction (Section 4.1-4.3), and by performing a fit to the whole X-ray band with the inclusion of a soft component (Section 4.4).

Abell S1101, also known as Sèrsic 159-03, is located at R.A.=23h13m58.5s, Dec.= -42d43m39, and the redshift is $z=0.058$; for a cosmology of $H_0 = 73 \text{ km s}^{-1} \text{ Mpc}^{-1}$, $\Omega_M = 0.27$, $\Omega_\Lambda = 0.73$, the distance to the cluster is $D_A = 220 \text{ Mpc}$, and 1 arcmin corresponds to 64 kpc. The paper is structured as follows: in Section 2 we describe the data reduction methods, in Section 3 we determine the temperature profiles of the clusters from the various observations, in Section 4 we determine the presence of a soft component above the hot ICM model, in Section 5 we provide a discussion on the possible origin of the excess emission, and in Section 6 we present our conclusions. Throughout the paper errors are quoted at the 1- σ , or 68% confidence level, unless otherwise stated.

2. DATA AND DATA ANALYSIS

In this Section we describe the *Chandra*, *XMM-Newton* and *ROSAT* observations of Abell S1101, and the method of analysis of the spatially resolved spectroscopy.

2.1. Chandra observations

We analyzed *Chandra* observation 11758 of exposure time 98 ks with the ACIS-I detector. The data were processed following the method described in Bonamente et al. (2006), which consists of filtering the observations for possible periods of flaring background, and applying the latest calibration; no significant flares were present in this observation. The reduction was performed in CIAO, using CALDB 4.1.3. The best-fit temperature of galaxy clusters depends on the effective area and the calibration of ACIS, which has changed throughout the mission (e.g., Reese et al. 2010), but low-temperature clusters such as Abell S1101 are largely unaffected by the details of the calibration, which impacts primarily the temperature of clusters at $kT \geq 5 \text{ keV}$ (see e.g. Nevalainen et al., 2010).

The background is measured from blank-sky datasets that are processed following the same method as the cluster observation (Markevitch et al. 2003). The blank-sky observations are first rescaled according to the high-energy flux of the cluster, to ensure a correct subtraction of the particle background that is dominant at $E > 9.5 \text{ keV}$, where the *Chandra* detectors have no effective area. The spectrum of a peripheral region of the observation, beyond 10 arcmin of the cluster center, is then accumulated; in this region little cluster emission is expected, and therefore we can check whether there is an enhancement of the soft X-ray background which could be in principle mistaken for cluster emission. In this observation we measure no detectable soft X-ray background enhancement, and therefore no additional processing of the blank-sky background is needed.

2.2. XMM-Newton observations

We analyzed the pn and MOS data of two *XMM-Newton* observations, 0123900101 and 0147800101. In

both observations, a thin optical blocking filter was used. We processed the raw *XMM-Newton* data with the SASv10.0.0 tools *epchain* and *emchain* with the default parameters in order to produce the event files. We used the latest calibration information as of September 2010. We also generated the simulated out-of-time event file, which we later used to subtract the events from the pn spectra registered during the readout of a CCD. We filtered the event files excluding bad pixels and CCD gaps. We further filtered the event files including only patterns 0–4 (pn) and 0–12 (MOS). To minimize the contamination of solar particle flares, we used the $>10 \text{ keV}$ ($> 9.5 \text{ keV}$) light curves for the pn (MOS) to accept data only from such periods when the count rate is within $\pm 20\%$ of the quiescent level. The resulting total exposure time is 85 ks and 222 ks for the pn and combined MOS1+MOS2.

We used the *evselect-3.60.6* tool to extract spectra, images, and light curves, while excluding the regions contaminated by bright point sources. We used the *rmfgen-1.55.2* and *arfgen-1.77.2* tools to produce the energy redistribution files and the effective area files. When running the *arfgen* tool, we used an extended source configuration and supplied an *XMM-Newton* image of the cluster in detector coordinates, binned in 0.5 arcmin pixels, for weighting the response.

We used the blank sky-based estimates for the total sky+particle background spectra from Nevalainen et al. (2005). In order to account for the variability of the instrumental background due to cosmic rays, we used the sample of EPIC exposures taken with a *CLOSED* filter (Nevalainen et al. 2005) to extract particle background spectra at the same detector regions as used for the cluster data. We included this additional component in the fits after adjusting its normalisation so that the total background count rate prediction in the 10–14 keV (9.5–12 keV) band for the pn (MOS) matches that in the cluster observation.

2.3. ROSAT observations

We analyzed *ROSAT* observation 800397 with the Position Sensitive Proportional Counter (PSPC) detector, for 13 ks of exposure. Data reduction was performed with XSELECT and the FTOOLS, following the prescriptions of Snowden et al. (1994), also described in Bonamente et al. (2002). In particular we removed periods of high particle background (master veto rate $\leq 170 \text{ counts s}^{-1}$) to improve the S/N of the data. Given the large field of view ($\sim 60 \text{ arcmin}$ radius), the PSPC provides a local background for this observation of Abell S1101, which is the most accurate for the spectral analysis. In particular, the local background estimate, obtained simultaneously with the cluster data, enables accurate removal of the time-variable Solar wind charge exchange contamination (e.g., Wargelin et al. 2004).

The PSPC detector has a unique feature that makes it especially suitable for the detection of soft X-ray radiation from clusters: a large ($\sim 200 \text{ cm}^2$) and well calibrated effective area below the Carbon edge ($\sim 0.28 \text{ keV}$). The R2 band, composed of pulse-invariant channels 20-41 and sometimes referred to as the 1/4 keV band, is sensitive to photons in the $\sim 0.2\text{--}0.4 \text{ keV}$ band, and is the band of choice to check for the presence of the soft excess emission in Abell S1101. This band is nominally present also in *Chandra*/ACIS and *XMM-*

Newton/MOS and PN, but calibrations uncertainties and low effective area prevent their scientific use in these two instruments.

2.4. Data analysis

Spectra were accumulated in annuli spaced by 2 arcmin radius, to match the resolution of the *ROSAT* PSPC which has an approximate resolution of ≤ 1 arcmin at all energies. We model the spectra using the APEC thermal model (Smith et al. 2001), with Wisconsin Galactic absorption cross-sections (Morrison & McCammon 1983) and Anders & Grevesse (1989) abundances; in Section 4 we present results using an alternative set of cross-sections (Balucinska-Church & McCammon 1992), showing that the choice of cross-sections is not crucial for the determination of soft X-ray fluxes. For *Chandra* and *XMM-Newton* spectra we let the abundance be a free parameter; for *ROSAT* we fix the abundances as explained in Sections 3 and 4. For *Chandra* and *XMM-Newton* data we only use the 0.7-7 keV band, and avoid the use of their lowest-energy channels which are more significantly affected by calibration uncertainties, and higher background. For *ROSAT*, we use the 0.2-2 keV band (PI channels 20-201), as described in Bonamente et al. (2002).

3. SPECTRAL FITS AND BANDPASS DEPENDENCE OF THE TEMPERATURE PROFILE

Presence of a soft component in the spectra of galaxy clusters will result in a bandpass dependence of the best-fit temperature, with softer bands returning a lower best-fit temperature than high-energy bands (Cavagnolo et al. 2008; Lehto et al. 2010). Also, an energy dependent calibration problem can produce a similar effect (Nevalainen et al. 2010).

To address the calibration of *Chandra* and *XMM-Newton*, we first fitted the *Chandra* and *XMM-Newton* spectra in the wide band (0.7-7.0 keV) and hard band (2.0-7.0 keV), using a single-temperature APEC model. We found that in the hard band the temperatures are consistent between the two instruments, as shown in Tables 1 and 2, and Figure 1 (the largest difference is at less than the $3\text{-}\sigma$ level in one bin, for a ratio between *Chandra* and *XMM-Newton* temperatures of 0.903 ± 0.037). Agreement of hard-band temperatures was also found for a sample of clusters observed with *Chandra* and *XMM-Newton* by Nevalainen et al. (2010), where it was shown that the bremsstrahlung temperatures agree with the Fe XXV/XXVI line ratio temperatures. It is therefore likely that the hard band calibration of *XMM-Newton* and *Chandra* does not have significant energy-dependent problems.

In the wide band, however, the temperatures obtained using *XMM-Newton* are systematically and significantly lower than those obtained with *Chandra* (see Figure 2 and Tables 1 and 2). Again, this is consistent with the analysis of the *XMM-Newton* - *Chandra* sample (Nevalainen et al. 2010) and is likely the result of remaining calibration uncertainties in the energy band ≤ 2 keV for any of the detectors.

Thus the comparison of the hard and wide band temperatures yields different results for *Chandra* and *XMM-Newton*: the best-fit *Chandra* temperatures in the whole X-ray band and in the hard band are statistically con-

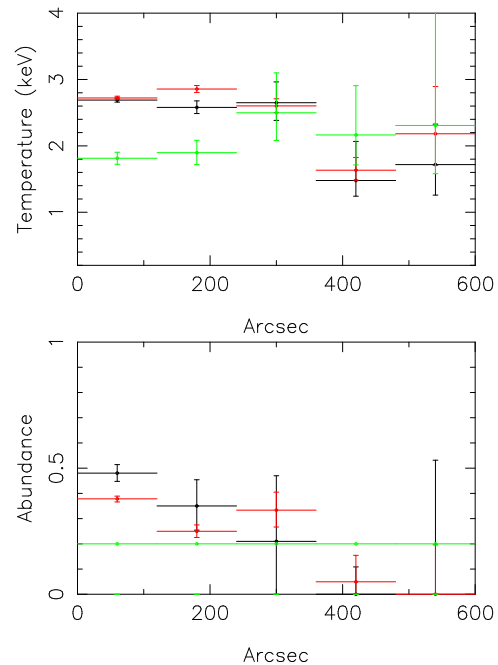


FIG. 1.— Temperature and abundance profiles in hard X-ray band (2-7 keV). Black: *Chandra*; Red: *XMM-Newton*. Overplotted are also the whole band (0.2-2 keV) results for *ROSAT* (green).

sistent at all radii, indicating that there is no discernible soft X-ray excess component at these energies (see Fig. 3). The *XMM-Newton* results differ from the *Chandra* results in that the wide-band fit detects a significantly lower temperature than the hard band (Figure 4), especially in the regions of highest S/N, consistent with the presence of soft excess in this cluster, as reported by Bonamente et al. (2005). Thus, with the current calibration we cannot establish whether the 0.7-2 keV band has evidence for soft excess emission in both *Chandra* and *XMM-Newton*.

ROSAT wide band (0.2-2 keV) temperatures are significantly lower than the hard band temperatures of *Chandra* and *XMM-Newton* in the inner two regions, where the signal has the highest S/N. (see Figure 1 and Tables 1 and 3). Assuming that the *ROSAT* calibration is correct, with effective area calibration errors at less than 5% (e.g. Snowden et al. 1994; Beuermann 2008), this difference can be explained by the existence of an additional soft component emitting primarily in the *ROSAT* band, indicating that the soft excess is dominant at energies below 1 keV. The best-fit *ROSAT* wide band temperatures are consistent with those from *Chandra* and *XMM-Newton* in the other regions where the S/N is lower.

We also study the dependence of the *ROSAT* temperature profiles on the assumed abundance profile, given that we cannot measure it directly from the *ROSAT* data themselves. We find that the two abundance profiles used (a decreasing one and a constant one), have negligible effect on the best-fit temperatures, especially given the statistical quality of the data (see Table 3).

4. MEASUREMENT OF SOFT EXCESS FLUXES

Since we are unable to determine conclusively whether there is excess emission in the *Chandra* or *XMM-Newton* 0.7-2 keV band of these Abell S1101 observations, and given the evidence for an additional emission component

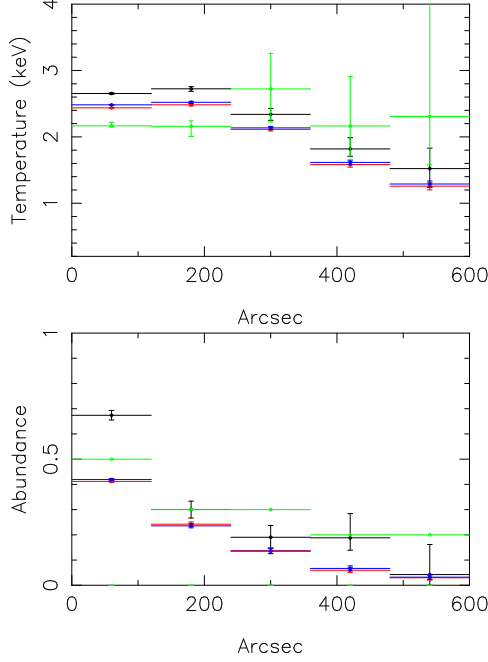


FIG. 2.— Temperature and abundance profiles in whole X-ray band. Black: *Chandra* (0.7-7 keV); Red: *XMM-Newton* (0.7-7 keV); Green: *ROSAT* (0.2-2 keV); blue: all instruments combined.

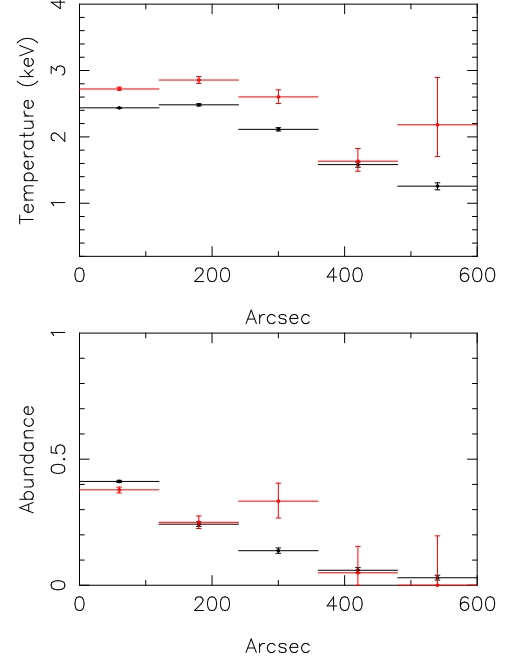


FIG. 4.— *XMM-Newton* temperature and abundance profiles in whole X-ray band (black), compared with profiles in hard band (red, 2-7 keV).

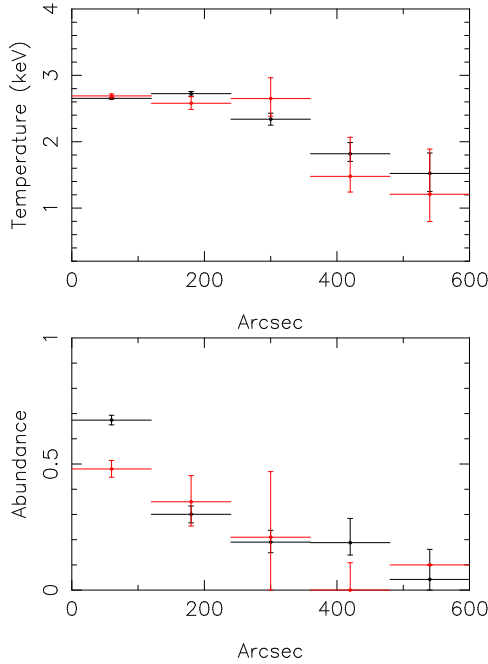


FIG. 3.— *Chandra* temperature and abundance profiles in whole X-ray band (black), compared with profiles in hard band (red, 2-7 keV).

in the lowest *ROSAT* channels provided in Section 3, we proceed to the analysis of the soft excess in the 1/4 keV *ROSAT* band (R2, 0.2-0.4 keV). In Section 4.1 we calculate soft excess fluxes using an extrapolation from the hard band model, following a procedure we used in earlier papers (e.g. Bonamente et al. 2005; Nevalainen et al. 2003; Bonamente et al. 2002). We then calculate the soft excess from fits that include the entire 0.7-7 keV *Chandra/XMM-Newton* bandpasses (Section 4.2), and con-

Annulus			
<i>Chandra</i> 0.7-7 keV fit			
(arcmin)	kT (keV)	A	χ^2 (d.o.f)
0-2	$2.65 \pm_{-0.01}^{+0.01}$	$0.67 \pm_{-0.02}^{+0.02}$	647.12 (413)
2-4	$2.72 \pm_{-0.03}^{+0.03}$	$0.30 \pm_{-0.03}^{+0.03}$	445.35 (422)
4-6	$2.34 \pm_{-0.09}^{+0.09}$	$0.19 \pm_{-0.04}^{+0.03}$	375.57 (429)
6-8	$1.82 \pm_{-0.12}^{+0.17}$	$0.19 \pm_{-0.05}^{+0.10}$	475.17 (429)
8-10	$1.52 \pm_{-0.27}^{+0.37}$	$0.04 \pm_{-0.04}^{+0.04}$	453.47 (420)
<i>Chandra</i> 2-7 keV fit			
(arcmin)	kT (keV)	A	χ^2 (d.o.f)
0-2	$2.69 \pm_{-0.03}^{+0.03}$	$0.48 \pm_{-0.03}^{+0.03}$	334.16 (324)
2-4	$2.58 \pm_{-0.09}^{+0.10}$	$0.35 \pm_{-0.10}^{+0.10}$	332.08 (333)
4-6	$2.65 \pm_{-0.27}^{+0.31}$	$0.21 \pm_{-0.21}^{+0.26}$	305.73 (340)
6-8	$1.48 \pm_{-0.24}^{+0.59}$	$0.00 \pm_{-0.00}^{+0.11}$	381.04 (340)
8-10	$1.21 \pm_{-0.41}^{+0.68}$	$0.10 \pm_{-0.00}^{+0.00}$	338.31 (331)
<i>XMM-Newton</i> 0.7-7 keV fit			
(arcmin)	kT (keV)	A	χ^2 (d.o.f)
0-2	$2.44 \pm_{-0.01}^{+0.01}$	$0.41 \pm_{-0.00}^{+0.00}$	2230.33 (1765)
2-4	$2.48 \pm_{-0.02}^{+0.02}$	$0.24 \pm_{-0.01}^{+0.01}$	974.86 (1043)
4-6	$2.11 \pm_{-0.02}^{+0.02}$	$0.14 \pm_{-0.01}^{+0.01}$	690.69 (723)
6-8	$1.58 \pm_{-0.04}^{+0.04}$	$0.06 \pm_{-0.01}^{+0.01}$	554.84 (571)
8-10	$1.26 \pm_{-0.06}^{+0.05}$	$0.03 \pm_{-0.01}^{+0.01}$	521.85 (574)
<i>XMM-Newton</i> 2-7 keV fit			
(arcmin)	kT (keV)	A	χ^2 (d.o.f)
0-2	$2.72 \pm_{-0.02}^{+0.03}$	$0.38 \pm_{-0.01}^{+0.01}$	918.25 (1063)
2-4	$2.86 \pm_{-0.05}^{+0.05}$	$0.25 \pm_{-0.02}^{+0.03}$	293.64 (429)
4-6	$2.60 \pm_{-0.10}^{+0.07}$	$0.33 \pm_{-0.07}^{+0.07}$	213.96 (276)
6-8	$1.63 \pm_{-0.15}^{+0.19}$	$0.05 \pm_{-0.05}^{+0.11}$	255.13 (244)
8-10	$2.18 \pm_{-0.48}^{+0.71}$	$0.00 \pm_{-0.00}^{+0.20}$	203.04 (281)

TABLE 1
BEST-FIT TEMPERATURE PROFILES FROM *Chandra* AND *XMM-Newton*.

Annulus (arcmin)	<i>Chandra</i> 2-7/0.7-7 keV	<i>XMM-Newton</i> 2-7/0.7-7 keV	<i>Chandra/XMM-Newton</i> 0.7-7 keV	<i>Chandra/XMM-Newton</i> 2-7 keV
0-2	1.014 ± 0.013	1.117 ± 0.009	1.089 ± 0.005	0.988 ± 0.014
2-4	0.947 ± 0.037	1.151 ± 0.022	1.097 ± 0.016	0.903 ± 0.037
4-6	1.133 ± 0.131	1.231 ± 0.051	1.107 ± 0.045	1.019 ± 0.119
6-8	0.813 ± 0.236	1.032 ± 0.111	1.149 ± 0.094	0.905 ± 0.270
8-10	1.128 ± 0.412	1.735 ± 0.478	1.210 ± 0.236	0.787 ± 0.326

TABLE 2
RATIO OF TEMPERATURES FROM *Chandra* AND *XMM-Newton* DATA.

Annulus (arcmin)	<i>ROSAT</i> 0.2-2 keV fits		
	<i>kT</i> (keV)	<i>A</i>	χ^2 (d.o.f)
0-2	1.81 ± ^{0.09} _{0.09}	0.20	197.07 (161)
2-4	1.90 ± ^{0.19} _{0.18}	0.20	115.16 (104)
4-6	2.50 ± ^{0.60} _{0.42}	0.20	69.01 (60)
6-8	2.16 ± ^{0.44} _{0.45}	0.20	52.58 (47)
8-10	2.31 ± ^{7.93} _{0.73}	0.20	59.74 (45)
0-2	2.17 ± ^{0.05} _{0.05}	0.50	250.97 (161)
2-4	2.16 ± ^{0.08} _{0.15}	0.30	123.93 (104)
4-6	2.72 ± ^{0.54} _{0.20}	0.30	70.92 (60)
6-8	2.16 ± ^{0.74} _{0.45}	0.20	52.58 (47)
8-10	2.31 ± ^{7.93} _{0.73}	0.20	59.74 (45)

TABLE 3
BEST-FIT TEMPERATURE PROFILES FROM *ROSAT*.

firm the presence of soft excess emission. The physical characteristics of the soft emitter are determined in Sections 4.4 and interpreted in Section 5, by modelling the whole-band *Chandra*, *XMM-Newton* and *ROSAT* spectra with two components that simultaneously describe both the hot ICM emission and the soft excess emitter.

4.1. Soft X-ray fluxes from hard-band model

Given the evidence presented in Section 3 that the hard band calibration of *Chandra* and *XMM-Newton* is accurate, we proceed with obtaining a joint hard band temperature profile. This is accomplished by fitting simultaneously the 2-7 keV band data from *Chandra* and *XMM-Newton* with the addition of the 1-2 keV band data from *ROSAT*. We find that the normalization constant of the *Chandra*, *XMM-Newton* and *ROSAT* best-fit models, after taking into account exclusion regions, are consistent within 10% for all instruments. This result is consistent with the current estimate of the *XMM-Newton/Chandra* flux cross-calibration uncertainty of ~10% (Nevalainen et al. 2010). Results are presented in Figure 5 and Table 4, where we also report the percentage of total measured R2 band fluxes above the background, as measured from the same *ROSAT* observations. We extrapolate this temperature profile to the *ROSAT* R2 band, and determine the fractional soft excess flux as

$$\eta = \frac{\text{flux}(R2) - \text{model}(R2)}{\text{model}(R2)}$$

as defined in Bonamente et al. (2002). Uncertainties in the hard-band models are included in the calculation of the soft excess fluxes. The radial profile of the fractional R2 band emission indicates a low level (~10–20%) of excess emission at radii ≤ 6 arcmin, and no soft residuals beyond that radius (Figure 6). The fact that the soft emission at large radii is consistent with the hot gas prediction is also an indication that the Galactic soft X-ray background was properly subtracted.

The left-hand panel of Figure 7 shows the *Chandra*, *XMM-Newton* and *ROSAT* spectra in the 0-2 and 2-4 arcmin regions, with the best-fit model obtained by a fit to the hard band of the three instruments. The spectra illustrate three points: at $E > 2$ keV for *Chandra* and *XMM-Newton*, and $E > 1$ keV for *ROSAT*, the three instruments are consistent; at $E = 0.7 - 2$ keV, *Chandra* has no evidence for an excess emission while both *XMM-Newton* instruments do; and, in the softest band (0.2-0.4 keV), *ROSAT* appears to detect an excess of emission. Similar conclusions apply to the 4-6 arcmin region.

To test for the impact of cooler gas in the core, or the effect of projection of cooler gas from outer regions, we also use a two-temperature APEC model (see Table 5) in which the second thermal model is constrained to have the same abundance and half the temperature of the first model, as done also by Kaastra et al. (2003). In fact, we know from X-ray spectroscopy that gas in the core is not found to cool much below half the peak temperature (Tamura et al. 2001; Peterson et al. 2003). The exercise shows that the soft residuals are still present when using this multi-phase model (see Fig. 6, red curve in left panel). Therefore we conclude that cooler gas with temperatures within one half that of the virial gas cannot explain the soft X-ray radiation in the 1/4 keV band.

We also test for the effect of the cross-section of Galactic absorbers in the derivation of the soft excess fluxes. Throughout the paper, we used the cross-sections of Morrison & McCammon (1983) with the abundances of Anders & Grevesse (1989). Of particular relevance for the study of the soft excess is the cross-section of helium, which has been revised several times, for example by Yan et al. (1998). Recently the Balucinska-Church & McCammon (1992) cross-sections were also revised, and we test the presence of the soft excess by use of these cross-sections, in conjunction with the Grevesse & Sauval (1998) abundances. We fit the joint X-ray spectra to a single-temperature thermal model, and the results presented in Table 6 show that the Morrison & McCammon (1983) and the Balucinska-Church & McCammon (1992) models differ by less than 5% in the 1/4 keV band, and the excess is detected with high significance in both cases (see Fig. 6, green curve in left panel). We therefore conclude that uncertainties in the cross-section of absorbing gas is not a significant factor in the determination of soft X-ray fluxes.

4.2. Soft X-ray fluxes from whole-band fits

We also determine the soft excess flux in the R2 band when the hot ICM is determined from a whole-band fit. Given that the *Chandra* and *XMM-Newton* instrument have systematic differences in the 0.7-2 keV fluxes, we perform two separate fits: one to the 0.7-7 keV *Chandra*

plus 0.5-2 keV *ROSAT* data, and one to the 0.7-7 keV *XMM-Newton* plus 0.5-2 keV *ROSAT* data. Results are presented in Table 7 and in Figure 6 (right panel), and are qualitatively similar to those obtained from the hard-band model: soft excess emission in the R2 band is detected for the two inner annuli (0-4 arcmin) with a confidence $\geq 2\sigma$. These results provide further evidence for the presence of soft excess emission in the R2 band above the contribution from the hot ICM, regardless of calibration uncertainties in the 0.7-2 keV band between *Chandra* and *XMM-Newton*.

4.3. Free- N_H fits to the whole-band *Chandra*, *XMM-Newton* and *PSPC* data

Another possibility for the appearance of soft residual fluxes in the R2 band is the use of an incorrect Galactic column density. We therefore perform a fit to the combined *Chandra*, *XMM-Newton* and *ROSAT* spectra in the entire spectral range, including the R2 band for *ROSAT*, and show the results of our fit in Table 8. These fits result in no soft excess fluxes for all regions in the R2 band, and indicate that the Galactic N_H required to explain the *ROSAT* soft fluxes must be in the range $N_H = 7 - 9 \times 10^{20} \text{ cm}^{-2}$, or approximately 30% lower than the value of $1.15 \times 10^{20} \text{ cm}^{-2}$ measured by the Kalberla et al. (2005) survey. Based on *XMM-Newton* and *Suzaku* observation, Werner et al. (2007) finds that the best-fit N_H towards the central region of the cluster is consistent with the LAB value, i.e., there is no need for soft excess component there, and that the excess emission remains present at large radii when using the LAB N_H value (Durret et al. 2008). The difference between these results and those of Werner et al. (2007) for the innermost region may be explained with the use of the *ROSAT* data covering the 1/4 keV band.

4.4. Fit to whole-band *Chandra*, *XMM-Newton* and *PSPC* data with an additional soft model

We also fit the whole band spectra to the customary 2-APEC model representative of the hot gas, plus a soft component to model the soft excess emission. The soft models are an APEC plasma with zero abundance, an APEC plasma with $A = 0.3$ abundance, and a power-law model. For the hot gas, the normalization was left free among the three spectra; the normalization and the temperature, or spectral index, of the soft component were linked among the spectra. For all regions, the normalization of the thermal component at half the temperature of the peak ICM model is found to be consistent with zero. The results are shown in Table 9, and indicate that the addition of the soft model leads to a significant improvement of the fit, when compared to a fit to the same spectra without the soft model. Based on the goodness of fit, the data do not indicate a strong preference for any of the three models for the soft excess. We notice that the best-fit temperatures of the thermal model with $A = 0.3$ abundance are significantly lower than those of the model with primordial abundances. This is likely due to the fact that the soft component is truly ‘soft’, i.e., mainly present in the *ROSAT* 1/4 keV band, since emission from gas at $kT \geq 0.25 \text{ keV}$ has a stronger line contribution in the higher *Chandra* and *XMM-Newton* bandpass, apparently not present in the data. Representative cases of the fit to the 0-2 and 2-4 arcmin spectra

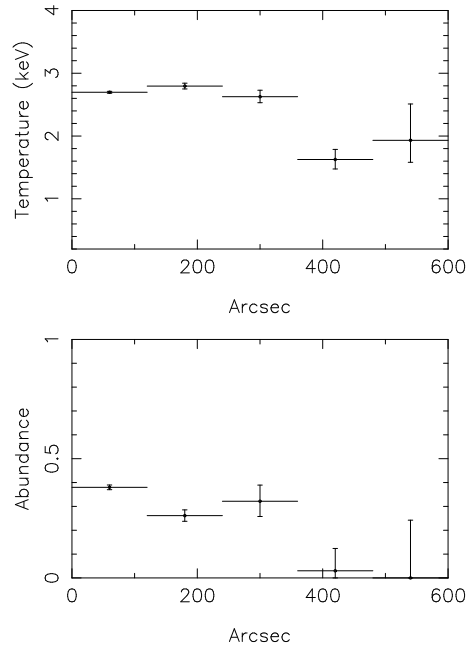


FIG. 5.— Temperature and abundance profile in high-energy band from composite *Chandra*, *XMM-Newton* and *ROSAT* high energy-data, using a single temperature model for the hot gas.

with the additional $A = 0$ thermal component are shown in the right-hand panels of Figure 7. The fact that *Chandra* and *XMM-Newton* do not agree in their 0.7-2 keV fluxes results in a slight overprediction of the 0.7-1 keV *Chandra* flux, while the *XMM-Newton* data in the same band are fit accurately by this model. Other models to the soft excess (the $A = 0.3$ thermal model and the non-thermal model) give similar results, and are not shown in Figure 7.

We calculate the soft excess fluxes associated with the $A = 0$ additional thermal component in the 0.3-1 keV band, and find them to be respectively 1.4, 1.5 and $0.7 \times 10^{-11} \text{ erg cm}^{-2} \text{ s}^{-1} \text{ deg}^{-2}$ for the three regions 0-2, 2-4 and 4-6 arcmin radius. These fluxes are lower than those found by Werner et al. (2007) based on *XMM-Newton* and *Suzaku* data, consistent with the fact that the new value of N_H implies reduced soft excess emission.

A source of uncertainty associated with these model fits is the choice of atomic physics included in the APEC model (Smith et al. 2001), which differ from other codes (e.g., the MEKAL/SPEX code, Mewe et al. 1985) for certain emission lines such as those of O VII. We tested this effect by fitting the 2-4 arcmin region using the MEKAL code for the warm component, and obtain a fit in which the best-fit temperature is $kT \leq 0.11 \text{ keV}$ (the MEKAL model covers the temperature range $kT \geq 0.081 \text{ keV}$), with a normalization of $0.61 \pm_{0.16}^{0.13}$ (in same units as those in Table 9), for $\chi^2_{min} = 1466.5$ for the same number of degrees of freedom as the APEC model. The fit has therefore the same statistical quality, and the higher best-fit temperature implies a reduced emission integral for the hot gas, since a cooler gas requires a higher emission integral to produce the same number of R2 band counts. The implications of this systematic uncertainty in the determination of the soft excess temperature are discussed in Section 5.

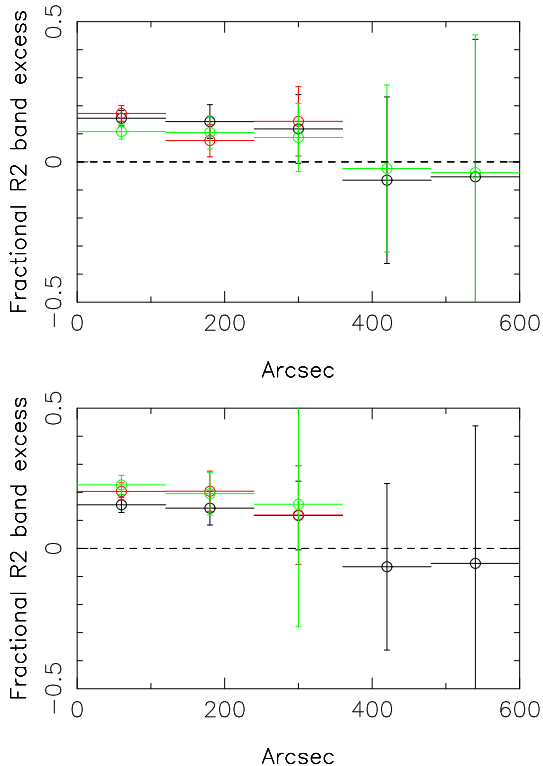


FIG. 6.— (Left) R2 band soft residual profile from high-energy composite *Chandra*, *XMM-Newton* and *ROSAT* fits. Black: fit is to a single APEC model with Morrison & McCammon (1983) cross-sections; Red: fit is to a two-APEC model with Morrison & McCammon (1983) cross-sections; Green: fit is to a single APEC model with Balucinska-Church & McCammon (1992) cross-sections. (Right) R2 band soft residual profile from whole-band fits to *Chandra* and *ROSAT* data (green) and *XMM-Newton* and *ROSAT* data (red); for comparison, in black are the residuals from the fit is to a single APEC model, as in left panel.

5. INTERPRETATION OF THE SOFT X-RAY FLUXES

Our results on the soft excess emission from Abell S1101 show that the cluster has a level of excess emission at the $\leq 20\%$ of the thermal virial gas, in agreement with the typical soft excess emission from a large sample of *ROSAT* clusters analyzed in Bonamente et al. (2002). In this Section we investigate two possible scenarios for the soft excess in Abell S1101, a thermal origin from diffuse filaments, and a non-thermal origin.

5.1. Thermal origin from large-scale filaments

An explanation for the excess emission in Abell S1101 and for the other *ROSAT* clusters analyzed in Bonamente et al. (2002) that feature a 10-20% soft excess, is that the emission originates from large-scale warm filaments seen in projections against the hot cluster gas. Filamentary structures of warm-hot intergalactic medium (WHIM) are routinely seen in numerical simulations of large scale structure formation (e.g. Davé et al. 2001), and even tentatively detected via their low surface brightness soft X-ray emission in a region between two neighboring galaxy clusters (Werner et al. 2008), and in the analysis of a sample of filaments of galaxies (Fraser-McKelvie et al. 2011), although the emission reported in the latter is in a higher energy band (0.9-1.3 keV). These filaments, are believed to contain a significant amount of the universe's baryons (e.g.

Cen 1998), and have a temperature ($T \sim 10^5 - 10^7$ K) that makes their detection very challenging. Attempts at their detection in absorption are likewise difficult (Zappacosta et al. 2005, 2010; Nicastro et al. 2005, 2010; Fang et al. 2010; Buote et al. 2009; Takei et al. 2007; Kaastra et al. 2006), primarily because it requires a bright source suitably located in their background, and the presence of metals. The filamentary origin was also studied in Bonamente et al. (2005) based on *XMM-Newton* data of Abell S1101, using the higher N_H value.

We use the thermal fits described in Section 4.4 to estimate the length of the putative filaments responsible for the soft emission component. We assume a simple geometry of cylindrical filaments of constant density directed along the line of sight, with footprints equal to the area of each annulus. In XSPEC, the emission integral of the putative warm gas is proportional to the normalization constant of the spectrum via

$$N = \frac{10^{-14}}{4\pi D_A^2 (1+z)^2} \int n_e n_H dV \text{ cm}^{-5} \quad (1)$$

where D_A is in cm, n_e and n_H are densities in cm^{-3} , $V = A \cdot L$ is the volume of the emitting gas, A the area of the annulus, and L the length along the sightline. We therefore use the normalization constant of the warm model to calculate the length L of the filaments, assuming a fiducial density of filament electrons of $n_{fil} = 10^{-4} \text{ cm}^{-3}$, and $n_e/n_H = 1.2$, appropriate for a highly ionized plasma with low metal abundances. The results, shown in Table 10, indicate that the filaments would be of order few Mpc, perhaps somewhat longer for the central region. Given that our estimates assume a constant filament density, and that the estimated length depends on the density as $L \propto N \propto n_{fil}^{-2}$, the length estimate for the central annulus would be reduced if the filaments are denser in that direction. A recent measurement of filament density by Fraser-McKelvie et al. (2011) finds that *ROSAT* observations in the direction of galaxy filaments is consistent with the emission from sub-virial gas at a density of few times 10^{-4} cm^{-3} , for a plasma temperature of 1 keV. If similar densities apply to the WHIM model presented in this paper, which features substantially lower temperatures, we calculate that a filament density $3 \times 10^{-4} \text{ cm}^{-3}$ would reduce the best estimates of the length towards the 0-2 arcmin region to a more plausible 3-5 Mpc.

Our estimates based on this analysis of *Chandra*, *XMM-Newton* and *ROSAT* data with the new N_H measurement of Kalberla et al. (2005) provide a scenario in which the soft X-ray emission from Abell S1101 is in fact consistent with an origin from relatively dense WHIM filaments. This re-analysis therefore brings Abell S1101 in line with the results obtained for a large sample of clusters observed by *ROSAT* (Bonamente et al. 2002), in which the excess emission is of the order 10-20% of that from the hot ICM. This thermal explanation was also found to be plausible for the large-scale halo of soft X-ray radiation around the brightest nearby cluster, the Coma cluster (Bonamente et al. 2003, 2009).

Our *ROSAT* soft X-ray data do not indicate strong preference between a thermal model of the warm gas with primordial abundances, or one with presence of metals ($A = 0.3$, see Table 9). We calculate limits to the pres-

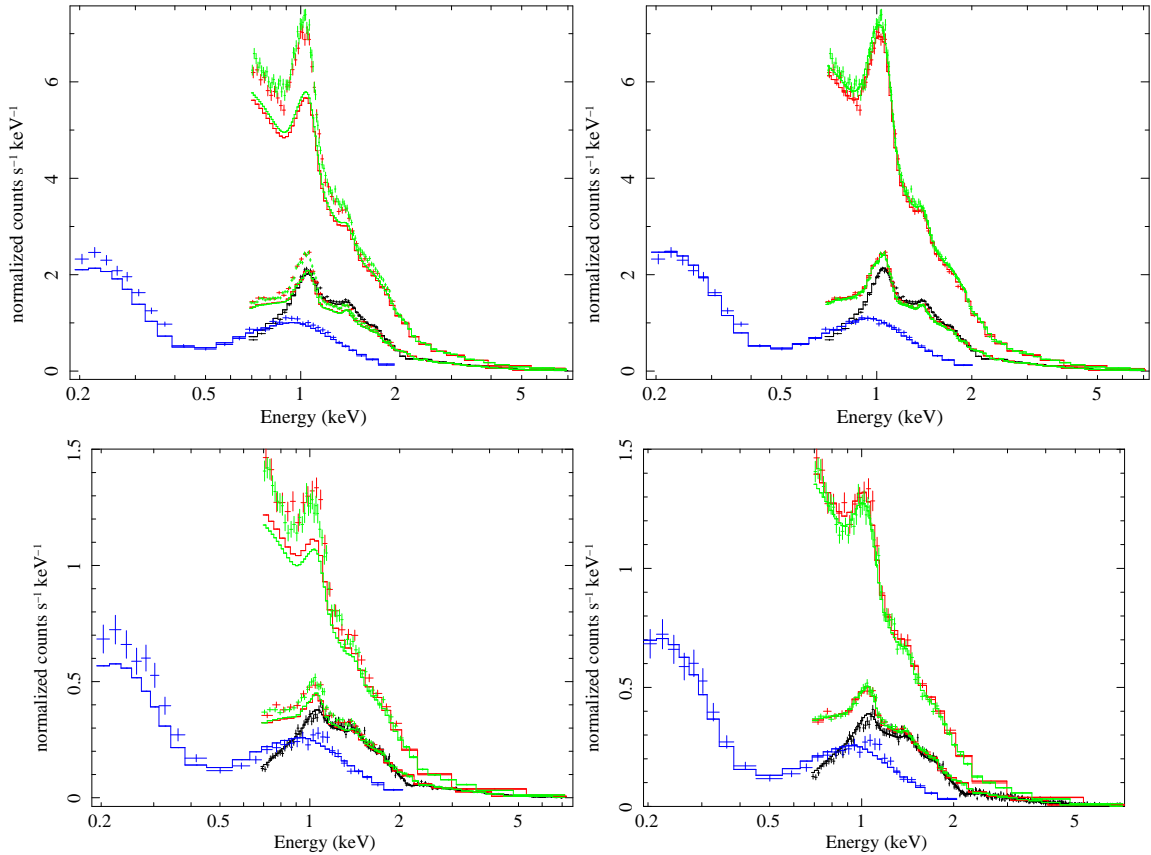


FIG. 7.— Top: Spectra of the region 0-2 arcmin; Bottom: Spectra of the region 2-4 arcmin. For both regions, *Chandra* spectra are in black, *XMM-Newton* in green (observation 0147800101)[†] and red (observation 0147800101), MOS is the lower set of curves, pn is the higher set, because of higher effective area, and *ROSAT* in blue. On the Left: Best-fit models are for the 1-APEC fit to the hard band, and the extrapolation to the soft band shows the excess emission above the hard band model. On the right: Best-fit models are for the 2-APEC model for the hot gas, plus a warm APEC model of fixed $A = 0$, as described in Table 9. Spectra were rebinned for clarity.

ence of O VII emission lines in the *ROSAT* data following the Werner et al. (2007) method by placing a narrow Gaussian emission line (of width parameter $\sigma = 0.1$ keV) at the expected line energy, above the non-thermal model described in Section 4.4. We calculate 2σ upper limits for the three regions of Table 9 as respectively 1.2, 1.4 and 1.0×10^{-6} photons $\text{cm}^{-2} \text{s}^{-2} \text{arcmin}^{-2}$, which are similar to the limits found by Werner et al. (2007).

A significant source of systematic error in the estimate of filament lengths is associated with the determination of the filament temperature. In fact, even the *ROSAT* soft X-ray band is not ideally suited for the measurement of temperatures below approximately a few times 100 eV. The intensity of emission lines from a plasma at sub-virial temperatures is also a source of uncertainty when measuring the temperature of warm gas. As an example of this source of uncertainty, in Section 4.4 we have shown that the 2-4 arcmin annulus excess, when fit to a MEKAL model instead of an APEC model, yields a higher filament temperature and an emission integral that is lower by one order of magnitude; this implies filament lengths that are lower by the same amount. Because of the difficulties in measuring the filament temperature, the filament lengths provided in Table 10 should be regarded only as order-of-magnitude estimates, e.g., these estimates could be significantly lower if the gas is at a somewhat higher temperature. Only a detection of specific emission lines from such ions as O VII will pro-

vide an accurate estimate of the temperature of the gas associated with the soft excess component.

The numerical simulations by Cheng et al. (2005) find that the soft excess emission may be explained with the presence of low-entropy, high-density gas, rather than the diffuse, high-entropy gas assumed in a WHIM filament model. Our observations do not have the resolution to probe whether the soft excess emitter is truly diffuse or localized in dense regions. If the Cheng et al. (2005) model is correct, the mass of warm gas required to explain the excess would be lower than that implied by the filament model.

5.2. Non-thermal origin of the soft excess

Inverse Compton scattering with a population of relativistic electrons can shift CMB photons to X-ray energies, and give rise to the soft excess emission (e.g. Sarazin & Lieu 1998; Bonamente et al. 2005; Lieu et al. 2010). A power-law distribution of cosmic ray electrons with differential number index μ generates a power-law spectrum with differential photon number index $\alpha = (\mu + 1)/2$. Therefore, the parameters of the power-law model described in Section 4.4 can be used to infer the energetics of relativistic electrons that may give rise to the soft excess.

In Table 10 we calculate the non-thermal pressure of the emitter, using the results of Table 9, and Equation 4 of Bonamente et al. (2005). For these calculations we use the measured non-thermal unabsorbed luminosities

of respectively 3.6, 2.9 and 2.2×10^{42} erg s $^{-1}$ for the three regions, in the *ROSAT* 0.2-2 keV band, and symmetric errors for the fit parameters. These estimates for the ratio of non-thermal to thermal pressure are lower than those based on the higher value of N_H (Bonamente et al. 2005; Werner et al. 2007), consistent with the reduction in soft excess fluxes because of the lower N_H value from the LAB survey. The result is that the putative non-thermal electrons would feature a pressure that is less than 1% of the thermal pressure, and therefore provide a marginal contribution to the overall cluster energetics.

6. CONCLUSIONS

In this paper we have presented spatially resolved X-ray spectroscopy of Abell S1101 with *Chandra*, *XMM-Newton* and *ROSAT*. Our observations show that calibration uncertainties in the 0.7-2 keV X-ray band remain between the *Chandra* and *XMM-Newton* detectors, with the *XMM-Newton* whole-band best-fit temperatures typically lower than those measured by *Chandra*, as also found by Nevalainen et al. (2010).

Our analysis confirms the presence of soft excess emission in the *ROSAT* 1/4 keV band, when the lower N_H value of Kalberla et al. (2005) is used, and regardless of calibration uncertainties between *Chandra* and *XMM-Newton* in the 0.7-2 keV band. The revised soft excess fluxes that we derived show that the level of soft X-ray excess emission in all clusters studied to date does not typically exceed $\sim 20\%$ of the hot gas emission in regions that are within the virial radius. In fact, using the scaling relation $r_{500} = (0.796 \pm 0.015)/(hE(z))(T/5\text{keV})^{(1.61 \pm 0.11)/3}$ Mpc from Vikhlinin et al. (2006), a $kT = 3$ keV cluster like Abell S1101 has $r_{500} \simeq 1$ Mpc, and the *ROSAT* 1/4 keV band excess is certainly within 6 arcmin, or ap-

proximately ~ 400 kpc; a similar situation applies to other clusters studied with *ROSAT* in Bonamente et al. (2002). A possible exception is the Coma cluster, for which we have shown that there is excess emission out to ~ 5 Mpc (Bonamente et al. 2009), and for a cluster at $kT = 8$ keV such as Coma, $r_{500} \simeq 1.9$ Mpc. The case of Coma may be exceptional in that it is one of the closest and brightest clusters, featuring higher S/N observations than any of the other clusters, and therefore it is possible that higher resolution soft X-ray observations near the virial radius may reveal that other clusters have soft X-ray halos that exceed the extent of the virialized gas.

The soft excess emission was interpreted as both thermal and non-thermal emission, and found that our data are consistent with both models for the excess. A possible origin for the soft excess is from WHIM filaments that are expected to converge towards massive galaxy clusters, and therefore become visible in X-rays even in the absence of metal lines. The best-fit temperature measured in this study are typically lower than the WHIM probed in other X-ray studies (e.g., Werner et al. 2008). In the case of a non-thermal origin, we find that the relativistic electrons responsible for the emission would feature a pressure of less than 1% of the thermal electrons. The upcoming launch of eRosita (Predehl et al. 2010), which improves on *ROSAT*'s large effective area at 1/4 keV and field of view, will enable further tests of the presence of warm gas near clusters such as the ones we have performed for this paper with *ROSAT*.

ACKNOWLEDGMENTS

The authors thank the referee for a thorough review of the manuscript and many suggestions that led to significant improvements to this paper.

REFERENCES

- Anders, E. & Grevesse, N. 1989, *Geochim. Cosmochim. Acta*, 53, 197
- Balucinska-Church, M. & McCammon, D. 1992, *ApJ*, 400, 699
- Beuermann, K. 2008, *A&A*, 481, 919
- Bonamente, M., Joy, M. K., LaRoque, S. J., Carlstrom, J. E., Reese, E. D., & Dawson, K. S. 2006, *ApJ*, 647, 25
- Bonamente, M., Joy, M. K., & Lieu, R. 2003, *ApJ*, 585, 722
- Bonamente, M., Lieu, R., & Bulbul, E. 2009, *ApJ*, 696, 1886
- Bonamente, M., Lieu, R., Joy, M. K., & Nevalainen, J. H. 2002, *ApJ*, 576, 688
- Bonamente, M., Lieu, R., & Mittaz, J. P. D. 2001, *ApJ*, 561, L63
- Bonamente, M., Lieu, R., Mittaz, J. P. D., Kaastra, J. S., & Nevalainen, J. 2005, *ApJ*, 629, 192
- Buote, D. A., Zappacosta, L., Fang, T., Humphrey, P. J., Gastaldello, F., & Tagliaferri, G. 2009, *ApJ*, 695, 1351
- Cavagnolo, K. W., Donahue, M., Voit, G. M., & Sun, M. 2008, *ApJ*, 682, 821
- Cen, R. 1998, *ApJ*, 498, L99
- Cheng, L.-M., Borgani, S., Tozzi, P., Tornatore, L., Diaferio, A., Dolag, K., He, X.-T., Moscardini, L., Murante, G., & Tormen, G. 2005, *A&A*, 431, 405
- Davé, R., Cen, R., Ostriker, J. P., Bryan, G. L., Hernquist, L., Katz, N., Weinberg, D. H., Norman, M. L., & O'Shea, B. 2001, *ApJ*, 552, 473
- Dickey, J. M. & Lockman, F. J. 1990, *ARA&A*, 28, 215
- Durret, F., Kaastra, J. S., Nevalainen, J., Ohashi, T., & Werner, N. 2008, *Space Science Reviews*, 134, 51
- Fang, T., Buote, D. A., Humphrey, P. J., Canizares, C. R., Zappacosta, L., Maiolino, R., Tagliaferri, G., & Gastaldello, F. 2010, *ApJ*, 714, 1715
- Fraser-McKelvie, A., Pimblett, K. A., & Lazendic, J. S. 2011, *ArXiv e-prints*
- Grevesse, N. & Sauval, A. J. 1998, *Space Sci. Rev.*, 85, 161
- Kaastra, J. S., Lieu, R., Tamura, T., Paerels, F. B. S., & den Herder, J. W. 2003, *A&A*, 397, 445
- Kaastra, J. S., Werner, N., Herder, J. W. A. d., Paerels, F. B. S., de Plaa, J., Rasmussen, A. P., & de Vries, C. P. 2006, *ApJ*, 652, 189
- Kalberla, P. M. W., Burton, W. B., Hartmann, D., Arnal, E. M., Bajaja, E., Morras, R., & Pöppel, W. G. L. 2005, *A&A*, 440, 775
- Lehto, T., Nevalainen, J., Bonamente, M., Ota, N., & Kaastra, J. 2010, *A&A*, 524, A70+
- Lieu, R., Ip, W.-H., Axoford, W. I., & Bonamente, M. 1999, *ApJ*, 510, L25
- Lieu, R., Mittaz, J. P. D., Bowyer, S., Breen, J. O., Lockman, F. J., Murphy, E. M., & Hwang, C.-Y. 1996a, *Science*, 274, 1335
- Lieu, R., Mittaz, J. P. D., Bowyer, S., Lockman, F. J., Hwang, C.-Y., & Schmitt, J. H. M. M. 1996b, *ApJ*, 458, L5+
- Lieu, R., Quenby, J., & Bonamente, M. 2010, *ApJ*, 721, 1482
- Markevitch, M., Bautz, M. W., Biller, B., Butt, Y., Edgar, R., Gaetz, T., Garmire, G., Grant, C. E., Green, P., Juda, M., Plucinsky, P. P., Schwartz, D., Smith, R., Vikhlinin, A., Virani, S., Wargelin, B. J., & Wolk, S. 2003, *ApJ*, 583, 70
- Mewe, R., Gronenschild, E. H. B. M., & van den Oord, G. H. J. 1985, *A&AS*, 62, 197
- Mittaz, J., Lieu, R., Cen, R., & Bonamente, M. 2004, *ApJ*, 617, 860
- Morrison, R. & McCammon, D. 1983, *ApJ*, 270, 119
- Nevalainen, J., David, L., & Guainazzi, M. 2010, *A&A*, 523, A22+

Annulus (arcmin)	Hot gas model		R2 band fluxes (c/s)			
	kT (keV)	A	detected flux 10^{-2} c/s	model flux	η	% above background
0-2	2.70 ± 0.02	0.38 ± 0.01	19.6 ± 0.4	17.0 ± 0.2	0.16 ± 0.05	98.0
2-4	2.80 ± 0.05	0.26 ± 0.02	6.7 ± 0.3	5.9 ± 0.2	0.14 ± 0.06	82.9
4-6	2.63 ± 0.10	0.32 ± 0.06	3.5 ± 0.2	3.1 ± 0.3	0.12 ± 0.12	59.4
6-8	1.63 ± 0.16	0.03 ± 0.09	2.4 ± 0.2	2.6 ± 0.6	-0.07 ± 0.30	40.1
8-10	1.93 ± 0.58	0.00 ± 0.24	1.4 ± 0.2	1.5 ± 0.5	-0.05 ± 0.50	22.6

TABLE 4

BEST-FIT *Chandra*, *XMM-Newton* AND *ROSAT* HOT GAS PARAMETERS IN HARD BAND (2-7 KEV FOR *Chandra* AND *XMM-Newton*, 1-2 KEV FOR *ROSAT*) AND R2 BAND FLUXES.

Annulus (arcmin)	kT (keV)	Hot gas model		R2 band fluxes (c/s)		
		1/2-kT fraction	A	detected flux 10^{-2} c/s	model flux	η
0-2	2.88 ± 0.07	0.37 ± 0.01	0.24 ± 0.06	19.6 ± 0.4	16.7 ± 0.2	0.17 ± 0.03
2-4	3.28 ± 0.18	0.25 ± 0.02	0.84 ± 0.28	6.7 ± 0.3	6.2 ± 0.3	0.08 ± 0.05
4-6	2.17 ± 0.19	0.33 ± 0.07	0.29 ± 0.16	3.5 ± 0.2	3.1 ± 0.3	0.14 ± 0.13

TABLE 5

BEST-FIT *Chandra* + *XMM-Newton* HOT GAS PARAMETERS AND R2 BAND FLUXES, USING THE 2-APEC MODEL WITH SECOND THERMAL COMPONENT FIXED AT 1/2 THE TEMPERATURE OF THE HOT COMPONENT.

Annulus (arcmin)	Hot gas model		R2 band fluxes (c/s)		
	kT (keV)	A	detected flux 10^{-2} c/s	model flux	η
0-2	2.80 ± 0.01	0.47 ± 0.01	19.6 ± 0.4	17.7 ± 0.2	0.11 ± 0.02
2-4	2.86 ± 0.04	0.32 ± 0.03	6.7 ± 0.3	6.1 ± 0.3	0.10 ± 0.06
4-6	2.69 ± 0.10	0.37 ± 0.08	3.5 ± 0.2	3.2 ± 0.3	0.09 ± 0.12
6-8	1.53 ± 0.21	0.09 ± 0.11	2.4 ± 0.2	2.5 ± 0.6	-0.02 ± 0.30
8-10	1.79 ± 0.53	0.13 ± 0.29	1.4 ± 0.2	1.4 ± 0.7	-0.04 ± 0.50

TABLE 6

BEST-FIT *Chandra* + *XMM-Newton* HOT GAS PARAMETERS AND R2 BAND FLUXES, USING THE BALUCINSKA-CHURCH & MCCAMMON (1992) CROSS-SECTIONS FOR GALACTIC ABSORBING MATERIAL .

Annulus (arcmin)	kT (keV)	A	detected flux 10^{-2} c/s	model flux	η	χ^2 (dof)
<i>XMM-Newton</i> plus <i>ROSAT</i>						
0-2	2.55 ± 0.01	0.43 ± 0.00	19.64 ± 0.41	16.32 ± 0.28	0.20 ± 0.03	2050.84 (1882)
2-4	2.56 ± 0.03	0.25 ± 0.01	6.70 ± 0.26	5.57 ± 0.30	0.20 ± 0.07	1009.08 (1106)
4-6	2.37 ± 0.06	0.16 ± 0.01	3.52 ± 0.22	3.15 ± 0.50	0.12 ± 0.17	678.93 (748)
<i>Chandra</i> plus <i>ROSAT</i>						
0-2	2.69 ± 0.01	0.46 ± 0.01	19.64 ± 0.41	16.01 ± 0.35	0.23 ± 0.03	763.34 (542)
2-4	2.74 ± 0.06	0.22 ± 0.02	6.70 ± 0.26	5.61 ± 0.33	0.20 ± 0.07	513.56 (497)
4-6	3.30 ± 0.96	0.11 ± 0.03	3.52 ± 0.22	3.04 ± 1.29	0.16 ± 0.43	409.64 (464)

TABLE 7

BEST-FIT HOT GAS PARAMETERS AND R2 BAND FLUXES, FROM A WHOLE BAND FIT (*XMM-Newton*, *Chandra*: 0.7-7 KEV; *PSPC*: 0.5-2 KEV).

Annulus (arcmin)	Hot gas model ($N_H = 1.15 \times 10^{20} \text{ cm}^{-2}$)			Free- N_H model		
	kT (keV)	A	χ^2 (dof)	kT (keV)	A	χ^2 (d.o.f)
0-2	2.60 ± 0.01	0.43 ± 0.01	2973.8 (2331)	2.64 ± 0.01	0.44 ± 0.01	0.85 ± 0.04 2837.0 (2330)
2-4	2.70 ± 0.04	0.24 ± 0.01	1542.8 (1560)	2.72 ± 0.02	0.25 ± 0.01	0.68 ± 0.07 1503.3 (1559)
4-6	2.38 ± 0.06	0.15 ± 0.01	1103.3 (1216)	2.39 ± 0.03	0.15 ± 0.01	0.84 ± 0.11 1097.3 (1215)

TABLE 8

BEST-FIT N_H VALUE OBTAINED BY A FIT TO THE *Chandra*, *XMM-Newton* AND *PSPC* WHOLE-BAND SPECTRA, USING THE 2-APEC MODEL WITH SECOND THERMAL COMPONENT FIXED AT 1/2 OF THE TEMPERATURE OF HOT COMPONENT.

Annulus (arcmin)	kT (keV)	Hot gas model		Soft component		χ^2 (dof)	Hot gas only
		A	Normalization				χ^2 (dof)
APEC model with $A = 0.0$							
				kT	Normalization		
0-2	$2.62 \pm_{-0.01}^{+0.01}$	$0.43 \pm_{-0.00}^{+0.00}$	19.14 ± 0.06	$0.10 \pm_{-0.03}^{+0.02}$	$11.77 \pm_{-2.79}^{+10.03}$	2827.3 (2329)	2896.7 (2331)
2-4	$2.73 \pm_{-0.02}^{+0.02}$	$0.26 \pm_{-0.01}^{+0.01}$	4.35 ± 0.04	$0.23 \pm_{-0.04}^{+0.04}$	$1.85 \pm_{-0.40}^{+0.53}$	1457.5 (1485)	1502.1 (1487)
4-6	$3.11 \pm_{-0.30}^{+0.19}$	$0.28 \pm_{-0.04}^{+0.08}$	0.84 ± 0.17	$1.00 \pm_{-0.37}^{+0.32}$	$0.80 \pm_{-0.19}^{+0.30}$	1070.8 (1203)	1094.1 (1205)
APEC model with $A = 0.3$							
				kT	Normalization		
0-2	$2.62 \pm_{-0.11}^{+0.01}$	$0.43 \pm_{-0.00}^{+0.00}$	19.15 ± 0.06	$0.06 \pm_{-0.01}^{+0.01}$	$7.54 \pm_{-7.04}^{+7.65}$	2822.0 (2329)	2896.7 (2331)
2-4	$2.69 \pm_{-0.03}^{+0.04}$	$0.24 \pm_{-0.01}^{+0.01}$	4.44 ± 0.03	$0.05 \pm_{-0.01}^{+0.03}$	$3.58 \pm_{-2.15}^{+2.04}$	1466.7 (1485)	1502.1 (1487)
4-6	$2.44 \pm_{-0.06}^{+0.07}$	$0.18 \pm_{-0.02}^{+0.02}$	1.84 ± 0.06	$0.23 \pm_{-0.04}^{+0.07}$	$0.12 \pm_{-0.06}^{+0.12}$	1082.7 (1203)	1094.1 (1205)
Power-law model							
				α	Normalization		
0-2	$2.63 \pm_{-0.01}^{+0.01}$	$0.44 \pm_{-0.01}^{+0.01}$	19.01 ± 0.12	$3.98 \pm_{-0.61}^{+0.79}$	$0.02 \pm_{-0.01}^{+0.03}$	2830.2 (2329)	2896.7 (2331)
2-4	$2.74 \pm_{-0.02}^{+0.03}$	$0.28 \pm_{-0.01}^{+0.01}$	4.16 ± 0.11	$2.72 \pm_{-0.23}^{+0.29}$	$0.06 \pm_{-0.02}^{+0.03}$	1449.0 (1485)	1502.1 (1487)
4-6	$2.33 \pm_{-0.14}^{+0.13}$	$0.19 \pm_{-0.02}^{+0.02}$	1.62 ± 0.09	$2.17 \pm_{-0.16}^{+0.23}$	$0.07 \pm_{-0.02}^{+0.02}$	1078.2 (1203)	1094.1 (1205)

TABLE 9

FIT TO A 2-APEC MODEL WITH SECOND THERMAL COMPONENT FIXED AT 1/2 THE TEMPERATURE OF THE HOT COMPONENT, PLUS AN ADDITIONAL SOFT COMPONENT (APEC, OR A POWER-LAW MODEL). FIT IS TO *Chandra*, *XMM-Newton* AND *PSPC* WHOLE-BAND SPECTRA. THE NORMALIZATION OF THE WARM THERMAL COMPONENT IS IN UNITS OF $10^{-11}/(D_A^2(1+z)^2) \int n_e n_H dV$, AND THE NORMALIZATION OF THE POWER-LAW MODEL IS IN UNITS OF 10^{+3} PHOTONS $\text{KEV}^{-1} \text{CM}^{-2} \text{S}^{-1}$ AT 1 KEV.

Annulus (arcmin)	Filament length (Mpc)		Average pressure ($10^{-11} \text{ erg cm}^{-3}$)	
	$A = 0$	$A = 0.3$	Hot ICM	Non-thermal component
0-2	48.00 ± 40.93	30.76 ± 31.19	26.0 ± 0.11	0.06 ± 0.06
2-4	2.52 ± 0.73	4.86 ± 9.58	4.78 ± 0.05	0.006 ± 0.002
4-6	0.66 ± 0.25	0.10 ± 0.10	1.54 ± 0.08	0.0015 ± 0.0005

TABLE 10

ESTIMATES OF FILAMENT LENGTH AND THERMAL-TO-NON THERMAL PRESSURE FOR THE MODELS OF TABLE 9. FILAMENT LENGTHS ASSUME $n = 10^{-4} \text{ cm}^{-3}$.

- Nicastro, F., Mathur, S., Elvis, M., Drake, J., Fiore, F., Fang, T., Fruscione, A., Krongold, Y., Marshall, H., & Williams, R. 2005, *ApJ*, 629, 700
- Peterson, J. R., Kahn, S. M., Paerels, F. B. S., Kaastra, J. S., Tamura, T., Bleeker, J. A. M., Ferrigno, C., & Jernigan, J. G. 2003, *ApJ*, 590, 207
- Predehl, P., Andritschke, R., Böhringer, H., Bornemann, W., Bräuninger, H., Brunner, H., Brusa, M., Burkert, W., Burwitz, V., Cappelluti, N., Churazov, E., Dennerl, K., Eder, J., Elbs, J., Freyberg, M., Friedrich, P., Fürmetz, M., Gaida, R., Hälker, O., Hartner, G., Hasinger, G., Hermann, S., Huber, H., Kendziorra, E., von Kienlin, A., Kink, W., Kreykenbohm, I., Lamer, G., Lapchov, I., Lehmann, K., Meidinger, N., Mican, B., Mohr, J., Mühlegger, M., Müller, S., Nandra, K., Pavlinsky, M., Pfeiffermann, E., Reiprich, T., Robrade, J., Rohé, C., Santangelo, A., Schächner, G., Schanz, T., Schmid, C., Schmitt, J., Schreib, R., Schrey, F., Schwöpe, A., Steinmetz, M., Strüder, L., Sunyaev, R., Tenzer, C., Tiedemann, L., Vongehr, M., & Wilms, J. 2010, in Presented at the Society of Photo-Optical Instrumentation Engineers (SPIE) Conference, Vol. 7732, Society of Photo-Optical Instrumentation Engineers (SPIE) Conference Series
- Reese, E. D., Kawahara, H., Kitayama, T., Ota, N., Sasaki, S., & Suto, Y. 2010, *ApJ*, 721, 653
- Sarazin, C. L. & Lieu, R. 1998, *ApJ*, 494, L177+
- Smith, R. K., Brickhouse, N. S., Liedahl, D. A., & Raymond, J. C. 2001, *ApJ*, 556, L91
- Snowden, S. L., McCammon, D., Burrows, D. N., & Mendenhall, J. A. 1994, *ApJ*, 424, 714
- Takei, Y., Henry, J. P., Finoguenov, A., Mitsuda, K., Tamura, T., Fujimoto, R., & Briel, U. G. 2007, *ApJ*, 655, 831
- Tamura, T., Kaastra, J. S., Peterson, J. R., Paerels, F. B. S., Mittaz, J. P. D., Trudolyubov, S. P., Stewart, G., Fabian, A. C., Mushotzky, R. F., Lumb, D. H., & Ikebe, Y. 2001, *A&A*, 365, L87
- Vikhlinin, A., Kravtsov, A., Forman, W., Jones, C., Markevitch, M., Murray, S. S., & Van Speybroeck, L. 2006, *ApJ*, 640, 691
- Wargelin, B. J., Markevitch, M., Juda, M., Kharchenko, V., Edgar, R., & Dalgarno, A. 2004, *ApJ*, 607, 596
- Werner, N., Finoguenov, A., Kaastra, J. S., Simionescu, A., Dietrich, J. P., Vink, J., & Böhringer, H. 2008, *A&A*, 482, L29
- Werner, N., Kaastra, J. S., Takei, Y., Lieu, R., Vink, J., & Tamura, T. 2007, *A&A*, 468, 849
- Yan, M., Sadeghpour, H. R., & Dalgarno, A. 1998, *ApJ*, 496, 1044
- Zappacosta, L., Maiolino, R., Mannucci, F., Gilli, R., & Schuecker, P. 2005, *MNRAS*, 357, 929
- Zappacosta, L., Nicastro, F., Maiolino, R., Tagliaferri, G., Buote, D. A., Fang, T., Humphrey, P. J., & Gastaldello, F. 2010, *ApJ*, 717, 74